

Research paper

Is ultralow friction on graphite sustainable in contaminated environments?

Hongyu Gao¹*, Sergey Sukhomlinov¹

Department of Materials Science & Engineering, Saarland University, Campus C6.3, Saarbrücken, 66123, Saarland, Germany



ARTICLE INFO

Keywords:

Structural lubricity
Surface contamination
Velocity-dependent friction
Molecular dynamics
Force-field development

ABSTRACT

Structural lubricity typically occurs in incommensurate, dry contacts where short-range elastic instability is minimized. Under ambient conditions, however, airborne molecules can adsorb onto solid surfaces, forming a viscous medium that alters interfacial properties. We hypothesize that despite the presence of physisorbed contaminants, structural lubricity on graphite can persist due to molecular ordering. Molecular dynamics simulations were performed with a newly parameterized interfacial potential to study *n*-hexadecane as a model contaminant on graphite surfaces. We investigated the effects of *n*-hexadecane coverage on shear stress, comparing behavior on graphite and gold (111). Results reveal that a monolayer of *n*-hexadecane molecules adheres strongly to graphite, replicating its lattice and maintaining solid-like behavior, which leads to orientation-dependent shear stresses. This behavior is absent on gold. As the contaminant film thickens, the orientation effect diminishes, and the shear stress-velocity relationship transitions from Coulomb to quasi-Stokesian and back to quasi-Coulomb as coverage increases. Despite a substantial increase in shear stress under ambient conditions, ultralow friction, or superlubricity, remains on graphite.

1. Introduction

Structural lubricity [1] refers to an ultra-low friction state that arises from the systematic annihilation of interfacial lateral forces due to lattice mismatch. In this context, interfacial atoms can be treated as the smallest contact units, with their energy states, driven by thermal motion, distributed stochastically across a potential energy landscape. Stokesian damping [2], which describes a linear increase in friction with sliding velocity, results from small perturbations of these interfacial atoms. This leads to primary energy dissipation as the atoms vibrate around their equilibrium positions within the lattice, without engaging in long-range elastic or quasi-discontinuous motion under shear forces. A scaling argument, based on the law of large numbers, dictates a sub-linear relationship between friction and contact area [3,4]: $F \propto A^n$, where the exponent n is capped at 0.5 and varies depending on the degree of lattice registry and geometric nature of the contact, including contact lines [1,5,6]. While this low-friction state is highly desirable, it can become unstable when the elastic correlation length is exceeded [7,8]. Beyond this threshold, structural defects, such as dislocations, can cause the sliding surfaces to interlock, significantly increasing shear stresses up to the Peierls stress limit [7].

Under ambient conditions, airborne molecules such as water and linear alkanes tend to adsorb onto solid surfaces, forming an orderly arranged monolayer that aligns with the underlying solid lattice [9]. With

prolonged exposure, this monolayer can develop into a nanometer-thick multilayer film [10], as indicated by an oscillatory density profile resulting from the liquid's wavenumber-dependent compressibility [11]. The anisotropic behavior of confined liquids, characterized by high in-plane molecular ordering, enables a load-bearing ability to a certain degree while still allowing molecular diffusion [11–13]. Interestingly, the presence of such an adsorption layer does not necessarily impede superlubricity¹ [14–16], with friction only mildly increasing alongside observations of rejuvenation, aging, and friction switches [16]. This suggests that earlier nano-manipulation experiments may have overlooked the existence of these layers, as contamination is unlikely to be fully eliminated, even under nominal ultra-high vacuum conditions. Unlike the constant velocity gradient typical of Couette flow, where molecules must overcome energy barriers due to steric hindrances, the shear plane in the boundary lubrication regime is located at heterojunctions with the lowest shear strength, exhibiting solid-like behavior. Consequently, when sliding occurs over such a viscoelastic medium, the frictional dependence on sliding speed is expected to be sub-linear [17].

Building on our previous studies [6,18], we focus on highly oriented pyrolytic graphite (HOPG) due to its superior performance as a solid lubricant. The aim is to examine the extent to which superlubricity is maintained in the presence of linear alkanes, specifically *n*-hexadecane

* Corresponding author.

E-mail address: hongyu.gao@uni-saarland.de (H. Gao).¹ Superlubricity is a broader term that encompasses ultralow friction states resulting from various mechanisms, including the presence of intermediate lubricious substances or incommensurate interfaces. In this context, structural lubricity can be considered as a subset of superlubricity.

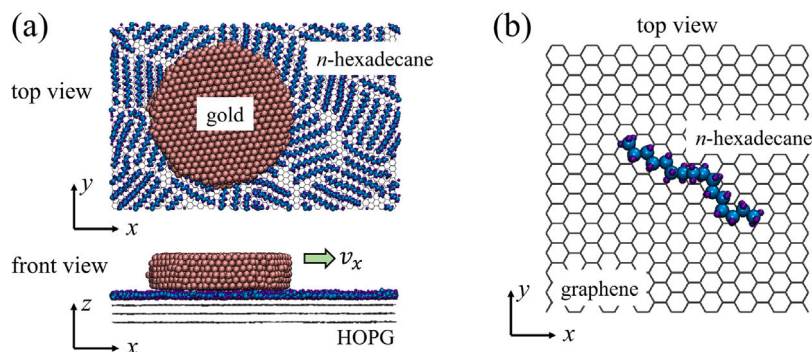


Fig. 1. Snapshots of (a) a representative sliding model system, showing a gold island sliding on a HOPG substrate coated with a monolayer of *n*-hexadecane molecules, and (b) a single-molecule-on-graphene model used for force field development.

(HEX), as a representative adsorption contaminant. To replicate the experimentally observed morphology of parallel stripes of HEX, with their longitudinal axes aligned parallel to the zigzag direction of HOPG, we reparameterized the interatomic interaction between HOPG and HEX based on density-functional theory (DFT) calculations. To validate this new parameter set, we calculated binding and desorption energies and compared them with experimental measurements. We then investigate how topography influences molecular in-plane ordering during liquid confinement. Finally, we study energy dissipation both in area-filling buried interfaces and at contact lines within the boundary lubrication regime. This study provides fundamental insights into the molecular mechanisms of friction and energy dissipation in the presence of adsorbed contaminants, which is critical for advancing the understanding of superlubricity under realistic conditions. Our findings may have practical implications for the design of advanced lubricants and coatings.

2. Methodology

Molecular desorption, liquid confinement, and boundary shearing are investigated using molecular dynamics (MD) simulations. The model systems consist of Au(111) and graphite (0001) (Gr) as solid surfaces, with *n*-hexadecane (HEX) as the adsorbent. It is important to note that graphite in ambient conditions is typically contaminated by a complex mixture of airborne molecules, including both low- and high-molecular-weight hydrocarbons, as demonstrated in prior experimental studies [19–21]. Nevertheless, this simplified model provides valuable insights into the fundamental mechanisms of superlubricity in the presence of adsorbed organic layers. A representative sliding model is shown in Fig. 1a. Detailed geometric parameters and operational conditions for each system are provided in the relevant sections to ensure clarity and reproducibility. The interactions within the system are described using the following potentials: the EAM [22] for Au, the AIREBO potential [23] for Gr, and the L-OPLS force field [24,25] for HEX. Cross-interactions are modeled using Morse [26] and Lennard-Jones [27] potentials for Au-Gr and Au-HEX interactions, respectively. The interaction between Gr and HEX has been reparameterized based on a single-molecule-on-graphene model, as depicted in Fig. 1b, with further details discussed in the Results section.

Unless stated otherwise, the system temperature is maintained at 300 K using a Langevin thermostat with a damping factor of 0.1 ps. During sliding simulations, the thermostat is applied only along the *y*-axis (perpendicular to the sliding direction) to avoid interference with the dynamics of the sliding process. A simulation timestep of 1 fs is used for all cases. All MD simulations are carried out using the open-source code LAMMPS [28]. To ensure statistical reliability, a time autocorrelation function (ACF) analysis is conducted to determine the optimal data output frequency. Mean values and standard errors are calculated based on uncorrelated data sets extracted from the simulations.

3. Results and discussion

3.1. Interfacial potential development

3.1.1. Interfacial potential model and parameterization

The interfacial interaction between graphite (Gr) and *n*-hexadecane (HEX) is described using the Buckingham potential [29], formulated as:

$$E_{\text{int}} = Ae^{-r/\rho} - \frac{C}{r^6}, \quad (1)$$

where A , ρ , and C are fitting parameters optimized through force matching (FM). This potential provides a more precise representation of short-range repulsive interactions with an exponential form, derived from the interpenetration of closed electron shells, making it more suitable for modeling boundary shearing [30,31]. Reparameterizing these potential parameters, rather than relying on mixing rules [32,33] for the non-bonded Lennard-Jones (LJ) parameters from the OPLS force field, is crucial because the latter, designed for bulk phase properties, fails to accurately capture the interfacial interactions, leading to a significant underestimation of the energy corrugation barrier. Two sets of parameters for $C_{\text{Gr}} - C_{\text{HEX}}$ and $C_{\text{Gr}} - H_{\text{HEX}}$ were determined by reproducing DFT-calculated static molecular forces (f) and binding energy (ΔE , defined in Eq. (5)) using a single-molecule-on-graphene model system. Sixteen configurations ($N_{\text{conf}} = 16$) were considered, encompassing a range of both in-plane and out-of-plane relative positions between the two substances.

3.1.2. DFT calculations

First-principles DFT calculations were performed using the Gaussian and plane-waves methodology [34,35] within the *Quickstep* module of the open-source software CP2K [36,37]. A plane-wave cutoff of 900 Hartree was applied to achieve a force convergence tolerance of 10^{-5} atomic units (a.u.). κ -point sampling was employed along with periodic boundary conditions in all three dimensions. To minimize empirical influences, a van der Waals density functional (vdW-DF) [38] was used, combining exchange at the generalized-gradient approximation (GGA) level, correlation at the local density approximation (LDA) level, and a non-local correction for van der Waals interactions. Carbon and hydrogen atoms were described using a triple- ζ Gaussian basis set [39], paired with Goedecker-Teter-Hutter (GTH) pseudopotentials [40,41]. The results closely align with those obtained using other widely-used methods, such as Perdew–Burke–Ernzerhof (PBE) [42] with Grimme’s DFT-D3 [43] corrections for dispersion interactions.

3.1.3. Force matching and optimization via simulated annealing

In FM, the discrepancy between DFT and force-field (FF) calculations was quantified using a penalty function χ^2 , defined as:

$$\chi^2 = \frac{1}{D} \frac{\sum_{\alpha=1}^D \omega_{\alpha} \chi_{\alpha}^2}{\sum_{\alpha=1}^D \omega_{\alpha}}, \quad (2)$$

Table 1
Optimized Buckingham parameters for Gr-HEX interactions.

$i - j$	A_{ij} (eV)	ρ_{ij} (Å)	C_{ij} (eV·Å ⁶)
$C_{Gr} - C_{HEX}$	1.75	0.09	57.13
$C_{Gr} - H_{HEX}$	132.66	0.34	0.00

where D ($D = 4$) represents the dimensionality including three force components plus energy, and ω (with $\omega_{f_x} = \omega_{f_y} = 5 \times \omega_{f_z} = 0.1 \times \omega_{\Delta E} = 1.0$) denotes the weighing factors² determined based on their respective value spans. The term χ_α^2 is defined as:

$$\chi_\alpha^2 = \frac{1}{N_{\text{conf}}} \sum_{i=1}^{N_{\text{conf}}} \frac{(\psi_{i,\alpha}^{\text{FF}} - \psi_{i,\alpha}^{\text{DFT}})^2}{(|\psi_{i,\alpha}^{\text{DFT}}| + \Delta)^2}, \quad (3)$$

where $\Delta = \max_{i,\alpha}(|\psi_{i,\alpha}^{\text{DFT}}|)$ serves as a denominator adjustment to mitigate the impact of small values on fitting stability, and $\psi = \{f, \Delta E\}$ represents the physical properties being compared. The minimization of χ^2 was executed using Monte Carlo-based simulated annealing [44]. The optimization process involved 1 cycle with 500 iterations per cycle. The temperature schedule was dynamically adjusted using the equation:

$$\text{temp} = 0.001 \times [1 - \cos(\frac{2\pi \times i_{\text{iter}}}{n_{\text{iter}}})] \times \cos(\frac{\pi \times i_{\text{cyc}}}{2n_{\text{cyc}}}), \quad (4)$$

where i_{iter} and i_{cyc} denote the iteration and cycle indices, respectively. The acceptance criterion was determined by the Metropolis algorithm, with an ideal acceptance ratio of 0.4. Convergence was achieved when $\chi^2 \leq 10^{-3}$, where $\chi^2 = 0$ indicates perfect agreement between FF and DFT calculations. These conditions ensure a thorough exploration of the parameter space, balancing convergence speed and accuracy.

3.1.4. Evaluation of fitting accuracy and model limitations

Fig. 2 compares the results from DFT and FF calculations, showing that the newly parameterized Buckingham potential (red solid circles) outperforms others in accurately reproducing both molecular forces and energies. The corresponding potential parameters are listed in Table 1. Notably, the out-of-plane forces (f_z) estimated with the mixed OPLS-LJ potential were significantly underestimated (blue open circles in Fig. 2c), especially in the repulsive regime. As shown in Fig. 2d and supported by our previous study [45], the normal force component influences the energy barrier, thereby affecting lateral motion. Predictions based on the AIREBO potential (black open circles) are notably less accurate in this context.

Reproducing collective properties like energy differences and molecular forces is relatively straightforward compared to reproducing per-atom forces, which require much complex functional forms that we were unable to identify. Specifically, we recognize our limitations in developing bond-order many-body potentials, including parameterizing the embedded-atom method (EAM) [46] and Steele [47] potentials, to account for possible many-body effects resulting from CH/ π interactions [48] that induce electron density changes upon approach. At this stage, we disregard the electrostatic interaction between Gr and HEX, assuming the graphene sheet is electronically neutral. We did not pursue machine-learning techniques, despite their promise, as the results might not align with established physical principles. Although imperfections exist, our approach achieves the initial objective of developing simple yet accurate means for modeling interfacial dynamics on a large scale with minimal computational cost.

² The weighing factors are introduced to balance the contributions of different physical properties (e.g., force components and energy) to the fitting process. They account for differences in the value spans of these properties, ensuring that no single property dominates the fitting due to its larger magnitude. For example, a smaller weighing factor is applied to F_z compared to F_x to equalize their contributions to the penalty function χ^2 .

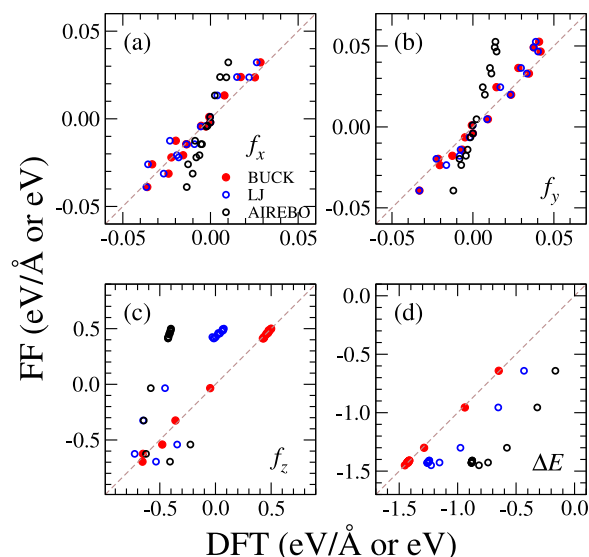


Fig. 2. Comparison between DFT- and force field (FF)-calculated molecular forces (f) along the (a) x -, (b) y -, and (c) z -direction, and (d) binding energy (ΔE). When $[\psi = \{f, \Delta E\}]^{\text{FF}} \equiv \psi^{\text{DFT}}$, the data points align precisely with the dashed lines. The Lennard-Jones (LJ) parameters were obtained using mixing rules on the all-atom L-OPLS parameters. The legend “BUCK” refers to the Buckingham potential. (For interpretation of the references to color in this figure legend, the reader is referred to the web version of this article.)

3.2. Physisorption of HEX on Gr

3.2.1. Binding energy and coverage density: Definitions and formulation

To validate the fitting parameters, we compared the binding energies (ΔE) required to dissociate a single HEX molecule from a Gr substrate with experimental data [49,50]. These energies were determined based on two equilibrium energy states, formulated as:

$$\Delta E = \langle E_{\text{bound}} \rangle - \langle E_{\text{sub}} + E_{\text{HEX}}^{\text{des}} \rangle \quad (5)$$

Here, E_{bound} represents the potential energy of the system when the target molecule is adsorbed on Gr, while E_{sub} and $E_{\text{HEX}}^{\text{des}}$ correspond to the potential energies of the substrate (including any remaining HEX molecules) and the desorbed molecule in isolation, respectively. The notation $\langle \rangle$ denotes a time average taken over a minimum duration of 10 ns. The coverage density (Γ) is determined by calculating the total in-plane occupation of HEX molecules, denoted as $m A_{\text{HEX}}^{\text{single}}$, where the projected area of a single HEX molecule ($A_{\text{HEX}}^{\text{single}}$) is approximately 105 \AA^2 [51]. Here, m represents the total number of molecules, which ranges from 1 to 30, corresponding to a Γ varying from 0.03 to 0.77 monolayers (ML).

3.2.2. Static binding energy and molecular arrangement

The MD-predicted binding energy for a single-molecule system ($m = 1$) is 1.08 eV, closely matching the value of 1.11 eV obtained from DFT calculations [52], where the influence of thermal effects appears to be negligible. As additional molecules aggregate in close proximity ($m > 1$), they arrange themselves in an orderly fashion, forming stripes with an average intermolecular spacing (Δl) of approximately 4.5 Å, as examples illustrated in Fig. 3(a) and (b). These adsorbed molecules adopt straight, all-*trans* configurations, favoring an orientation along the zigzag direction of the graphite substrate, which aligns with experimental observations [53]. Such a structural arrangement is energetically favorable, given that the periodicity along the graphene armchair direction is 4.26 Å, in close agreement with Δl .

Histograms showing the molecular orientation during dynamic equilibrium for two representative systems are presented in Fig. 3(c), where the orientation vectors are determined as the end-to-end vector of

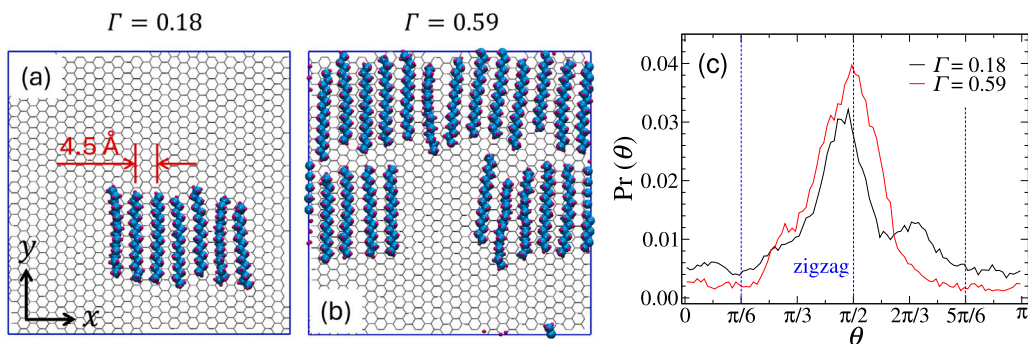


Fig. 3. Snapshots of model systems at equilibrium at 300 K with coverage densities of (a) $\Gamma = 0.18$ and (b) $\Gamma = 0.59$. The molecules align along the zigzag direction of graphene, maintaining an average intermolecular spacing of 4.5 Å. (c) Histograms showing the distribution of angles (θ) between the longitudinal orientation of the molecules and the x -axis during equilibration.

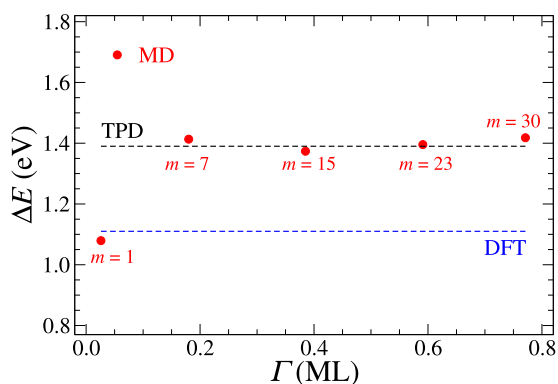


Fig. 4. Binding energy (ΔE) of HEX on Gr as a function of coverage density (Γ). The blue dashed line represents a DFT calculation [52] from the same setup. The value is extrapolated using the relation: $\Delta E(N_C) = -0.067N_C - 0.04$ eV, where N_C denotes the number of backbone carbons. The black dashed line indicates the desorption energy (ΔE_{des}) derived from the relationship $\Delta E_{des} = -29 + 42N^{0.5}$, based on temperature-programmed desorption (TPD) experiments [50]. Error bars are omitted as they are smaller than the symbol size. (For interpretation of the references to color in this figure legend, the reader is referred to the web version of this article.)

each molecule along the longitudinal direction. An increase in binding energy of approximately 0.5 eV is observed as the number of molecules m increases from one to numerous, as shown in Fig. 4. Beyond this point, ΔE remains constant as Γ further increases, regardless of the initial desorption position of the target molecule. This suggests that the binding energies obtained here correspond to the desorption of a molecule from the domain edges, which are preferred sites due to the low desorption energy barrier caused by structural asymmetry.

3.2.3. Dynamic desorption and energy barrier analysis

The binding energies presented in Fig. 4 (red solid circles) are consistent with the MD-modeled energy barriers obtained from continuous pulling of a single molecule from an adsorption state to an isolated state along the surface normal while maintaining a constant center-of-mass (COM) displacement rate of 0.05 m/s. During this process, no reattachment of detached fragments is observed, owing to the high persistence length of these short-chain molecules. The correlation between free energy and the number of detached fragments suggests minimal configurational changes between *trans* and *gauche* states. These values are also in agreement with the desorption barrier (ΔE_{des}) extracted from temperature-programmed desorption (TPD) experiments (represented by the black dashed line in Fig. 4), where the linearly interpolated peak desorption temperature (T_p) is approximately 308 K [49,50], close to the 300 K used in MD simulations. Our simulation results support the experimentally observed first-order desorption process, where the

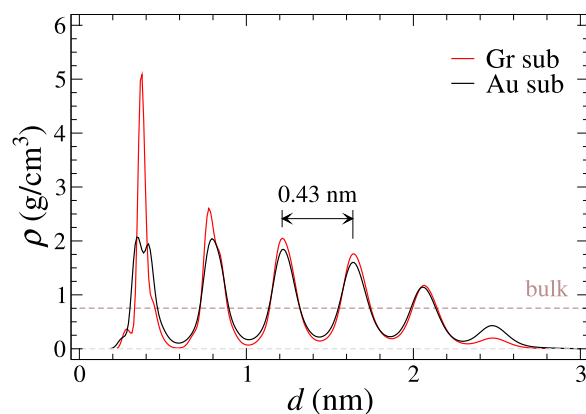


Fig. 5. Density profiles (ρ) of HEX films on graphite (Gr, red) and gold (Au(111), black) substrates along the surface normal. The simulation cell has an in-plane dimension of 11.5×11.6 nm². The surface of the substrate is set at $d = 0$ nm for both materials. The HEX films exhibit a characteristic density oscillation periodicity (λ) of approximately 0.43 nm in both cases. The number of molecules in the first monolayer is $m = 117$ on Au and 128 on Gr. (For interpretation of the references to color in this figure legend, the reader is referred to the web version of this article.)

desorption barrier is independent of coverage density, indicating relatively weak and short-ranged intermolecular interactions among the molecules. According to DFT calculations, the presence of oligomers on graphene could cause deviations in the electronic structure of graphene from the Fermi level observed in pristine graphene, resulting in an energy gap of up to 6 meV [52].

3.3. Nanoscale confinement and shearing

3.3.1. Solvation forces

When liquids are confined within nanoscale slits, they often form layered structures [54,55] as molecules self-organize with significant in-plane order due to the perturbative effect of solid surfaces. A solid surface can induce in-plane molecular ordering that extends through several molecular layers, manifesting in oscillatory density profiles that decay with distance from the solid-liquid interface. The in-plane ordering of HEX on Gr is notably more pronounced than on a Au(111) surface, as shown in Fig. 5. Specifically, the peak density of the HEX layer in immanent contact with Gr is nearly 2.5 times that on a Au(111) surface and 6.2 times that in a bulk phase. This structured, densely packed, anisotropic arrangement of molecules across neighboring layers can withstand substantial normal loads on the order of 100 MPa without necessitating a phase transformation from liquid to solid [11]. Additionally, the prolonged relaxation time observed in confined liquids, which is inversely related to shear viscosity, leads to noticeable

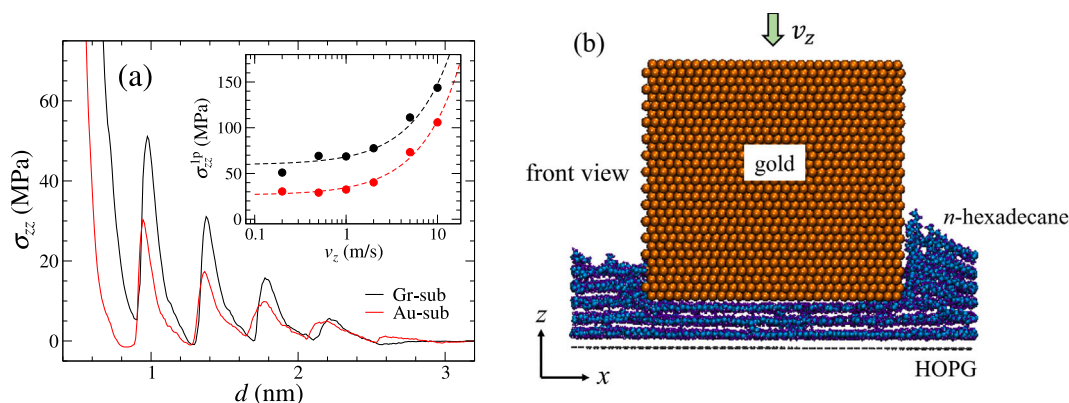


Fig. 6. (a) Normal stress (σ_{zz}) during a compression of a HEX film by a cylindrical Au(111) indenter with a radius of 3.7 nm. A snapshot of the simulation model during compression is shown in (b). The uppermost substrate surface is set at $d = 0$ nm, with in-plane dimensions of 11.5×11.6 nm². The indenter moves at a constant loading rate of $v_z = 0.2$ m/s. The inset of (a) shows the first stress peak (σ_{zz}^{1p}) as a function of the confining rate.

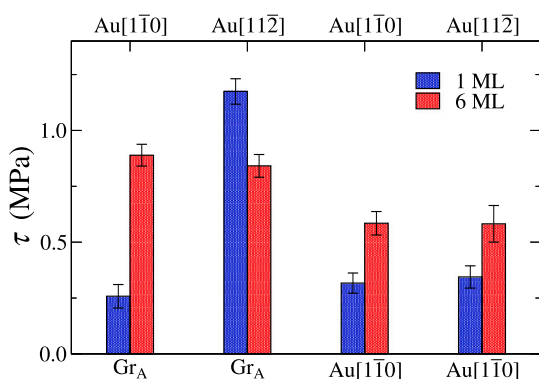


Fig. 7. Shear stress (τ) between two sliding slabs with an intermediate HEX film composed of either one (blue) or six (red) monolayers. The top and bottom ticks indicate the material types and lattice orientations aligned with the sliding direction of the respective slabs. The in-plane dimensions of the simulation cell are 6.4×6.4 nm², ensuring that the lattice difference-induced in-plane strain is less than 1% as an artifact. Atoms in the outermost layers of the solids are constrained to zero stress. The top slab slides at a constant speed of 10 m/s under only an adhesive load. Shear stresses in the Au-HEX-Gr cases are from REF [16]. (For interpretation of the references to color in this figure legend, the reader is referred to the web version of this article.)

hysteresis in stress relaxation [12], underscoring the complex dynamics at play in nano-confined liquid systems.

As a tip progressively approaches a substrate surface, the layer-by-layer squeezing out caused by in-plane molecular ordering leads to oscillatory solvation forces, with their magnitude influenced by the loading rate. As shown in Fig. 6, the peak normal stresses (σ_{zz}^p) during nominally steady-state compression ($v_z = 0.2$ m/s) increase exponentially as the confining distance (d) decreases, with a wavelength comparable to the interlayer distance. The slightly negative stresses at the valleys correspond to the transition where molecular layers are expelled from n to $n - 1$. Our results suggest that pushing the last layer of molecules (at $d < 0.9$ nm) outside the contact interface to achieve solid–solid contact requires substantial effort and may even be impossible, especially when the tips are blunt, resulting in a large aspect ratio. The heterogeneity of liquids under nanoscale confinement and the resulting stress anisotropy arise naturally from the liquid’s wavelength-dependent compressibility, which aligns with bulk-liquid density autocorrelation functions (ACF) [56,57], rather than the specific nature of the solid surfaces. However, detailed molecular arrangements are associated with surface topography; thus, σ_{zz} on Gr is notably higher due to the orientation-dependent higher Gr-HEX commensurability, which induces a higher corrugation barrier, making lateral displacement more difficult.

3.4. Shear stress

3.4.1. Shear stress in confined liquid films: Lattice effects and superlubricity

Shear stresses (τ), calculated as the ratio of lateral force (F) to the apparent contact area (A), are evaluated when a Au(111) slab slides against a HEX film situated atop a Gr substrate under an adhesive load. This loading condition is commonly employed in nanoisland manipulation experiments conducted in contact mode [14,16,45]. With a monolayer of HEX ($\Gamma \approx 0.8$), shear stresses exhibit a strong correlation with the lattice orientation of the confining solids. Specifically, as illustrated by the two leftmost blue bars in Fig. 7, τ is approximately five times higher when the gold’s [112] direction vector aligns parallel to graphene’s armchair direction (the sliding direction) compared to when its orthogonal vector, [110], aligns in the same direction. Note that the stresses reported in Fig. 7 are from area-filling contacts, which exclude the energy dissipation at the contact lines [6] or due to spontaneous cluster rotation [18].

In the presence of a single monolayer of HEX molecules, the orientation-dependent shear stresses exhibit solid-like behavior, with the HEX monolayer effectively mimicking the graphene lattice. The notable lattice congruency between Au(111) and Gr(0001), as depicted in Fig. 8b, facilitates the formation of Moiré patterns [6], which, with extended superlattice wavelengths, promote longer-range instabilities at small lattice mismatches characterized by an elevated stress–strain gradient. Although the presence of a HEX monolayer amplifies τ by nearly a hundredfold compared to gold sliding directly against graphite [6], it does not cause a breakdown of superlubricity. One reason is that this modeled large friction discrepancy would be significantly reduced at experimentally³ realistic sliding speeds, which are typically nine orders of magnitude lower, due to different friction-velocity dependence in the presence and absence of intermediate contaminants (discussed next). Additionally, the much larger contact area of nanoislands, on the order of $10^3 \sim 10^5$ nm² in experiments, will mitigate the effects of energy dissipation at contact lines caused by structural discontinuities [6] or molecular plowing [58].

In contrast, the orientation effect is not discernible in the Au-HEX-Au systems, as shown by the two rightmost blue bars in Fig. 7. This can be attributed to HEX’s low binding energy to Au(111) [59], which fails to foster the same degree of molecular ordering observed on graphite, even when the two solid slabs are commensurate, as evidenced by the less pronounced density peaks in Fig. 5. The orientation effect also diminishes as the HEX film thickness increases from one to six molecular layers, where viscous damping becomes increasingly dominant due to

³ Refers specifically to nanomanipulation experiments [14,16] conducted with AFM

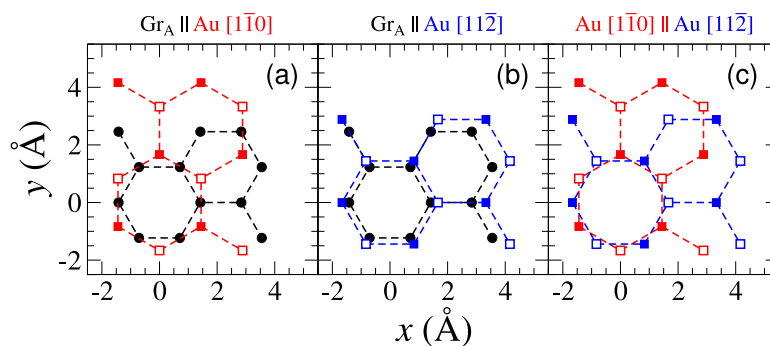


Fig. 8. Illustration of lattice structures and orientations of the solid counterfaces. The text above each sub-panel indicates the bottom and top slabs, respectively, along with their lattice orientations, positioned on the left and right of the \parallel sign. Solid and hollow square symbols represent Au atoms from two neighboring atomic layers. The sliding direction is along the $+x$ axis.

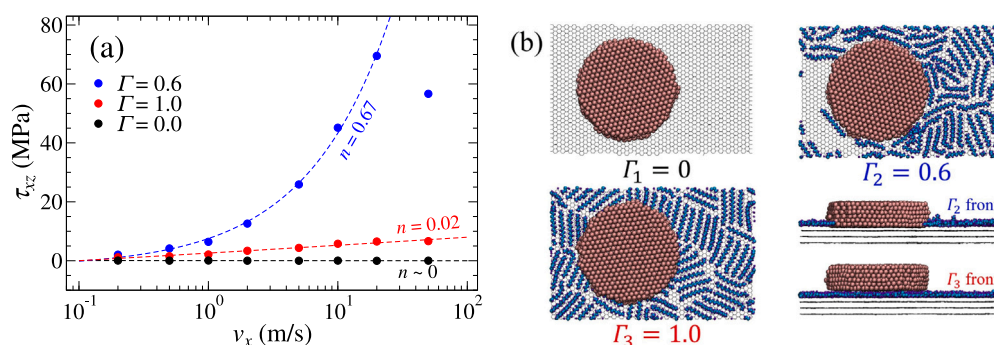


Fig. 9. (a) Velocity-dependent shear stress (τ_{xz}) during the sliding of a gold island on graphite (0001) at varying coverage densities (Γ) ranging from zero to one. The gold island has a cylindrical shape with a radius of 2.8 nm and a thickness of 1.0 nm. The in-plane dimensions of the HOPG are 11.5×7.4 nm². The island slides along the armchair direction of HOPG under an adhesive load, with its (111) surface parallel to the sliding plane. The rotational degrees of freedom of the island are allowed. Snapshots of the model systems are shown in (b). The dashed lines represent fitting with a power-law function, where n denotes the power-law exponent. The last data point in blue (at 50 m/s) is excluded from the fitting. (For interpretation of the references to color in this figure legend, the reader is referred to the web version of this article.)

the decay of in-plane molecular ordering with distance from the solid surfaces. As a result, the reduced interlayer lattice congruency renders the solid's lattice orientation insignificant, leading to comparable shear stresses (shown by the red bars in Fig. 7) between systems with low and high commensurability. However, shear stresses arising from elastic instability continue to surpass those from viscous stresses under conditions equivalent to shearing a bulk liquid in a Couette flow [18]. In the latter case, although molecules align along the streaming direction according to their anisotropic radius of gyration [18], their spatially-resolved density remains evenly distributed normal to the sliding plane rather than being oscillatory.

3.4.2. Sliding of gold nanoislands on contaminated HOPG: Speed and coverage effects

With a finite geometry, contributions from both inside and outside the contact are taken into account. Interestingly, as shown in Fig. 9a, shear stresses exhibit different dependence on sliding speed depending on the coverage density. In the absence of contaminants (dry contact, $\Gamma = 0$), the stresses (black symbols) are the lowest, with damping being Coulombic, as indicated by the power-law exponent n being nearly zero. When HOPG is lightly contaminated, meaning the island remains in direct contact with HOPG but with HEX molecules in close proximity ($\Gamma = 0.5$), the shear stresses (blue symbols) are the highest, mainly due to the energy dissipated at the leading edge as HEX molecules are displaced, overcoming the accumulated corrugation barrier. At low speeds, molecules have sufficient time to refill the sliding-induced vacancies at the trailing edge, while at high speeds, they cannot quickly flow back to the sliding trace due to hysteresis, leading to a quasi-Stokesian dependence ($n = 0.67$). In an extreme case, this can result in a drop in shear stress (at $v_x = 50$ m/s) during reciprocal sliding

when molecules cannot return in time at the leading edge. When a nearly full monolayer of contaminants forms such that the island floats on it, the shear stresses (red symbols) remain low and exhibit a weak dependence on sliding speed, consistent with experimental observations [60]. This behavior indicates that the monolayer is in a solid-like state, with closely packed and aligned molecules, persisting superlubricity or, alternatively, quasi-structural lubricity.

4. Conclusions

This study advances the understanding of structural lubricity by focusing on the impact of surface contamination [14,15,61], an underexplored area despite its significance in tribological systems. We specifically investigated the influence of airborne adsorbates on the lubricity of graphite (Gr) under ambient conditions, using *n*-hexadecane (HEX) as a model contaminant. To achieve a more accurate representation of atomistic interactions, a novel model was developed based on DFT-calculated molecular forces and binding energies, which improves the accuracy over conventional mixing rules [24]. Molecular dynamics simulations with this reparameterized potential successfully replicated desorption energies derived from temperature-programmed desorption experiments [50], confirming the robustness of the model and offering a more accurate depiction of surface interactions than prior approaches.

Our simulations revealed that HEX molecules adopt straight, all-*trans* configurations aligned with the zigzag direction of Gr, consistent with experimental observations [53]. This molecular arrangement forms a highly ordered, anisotropic structure where the HEX film undergoes a discontinuous, layer-by-layer expulsion under compression. Notably, the last monolayer exhibits solid-like behavior, with shear

stresses strongly dependent on the sliding orientation, a phenomenon absent on Au(111) surfaces. The lattice congruency between HEX and Gr provides novel insights into how atomic-scale surface interactions govern lubrication behavior. As the film thickness increases to several nanometers, the anisotropic effects of the monolayer diminish, marking a transition to a more homogeneous lubrication regime.

In comparison to existing literature, this work bridges the gap between molecular-scale simulations and practical engineering applications by elucidating the transition from Coulomb-like to Stokesian behavior on account of adsorbate coverage. These findings, supported by cutting-edge experiments [60], offer fresh insights for the design of protective coatings with enhanced lubrication properties, which could significantly impact the development of advanced materials in tribological systems. Future work should focus on extending these molecular insights to more complex material systems and surface conditions, while direct experimental validation of the simulation results will be crucial to further solidify the findings and their application to real-world scenarios.

CRedit authorship contribution statement

Hongyu Gao: Writing – review & editing, Writing – original draft, Visualization, Validation, Supervision, Software, Resources, Project administration, Methodology, Investigation, Funding acquisition, Formal analysis, Data curation, Conceptualization. **Sergey Sukhomlinov:** Writing – review & editing, Validation, Software, Methodology, Investigation.

Declaration of competing interest

The authors declare the following financial interests/personal relationships which may be considered as potential competing interests: Hongyu Gao reports financial support and travel were provided by German Research Foundation. If there are other authors, they declare that they have no known competing financial interests or personal relationships that could have appeared to influence the work reported in this paper.

Acknowledgments

We thank Martin Müser, Mehmet Baykara, Wengen Ouyang, and Wai Oo for useful discussions. This research was supported by the German Research Foundation (DFG) under grant numbers GA 3059/2-1 and GA 3059/4-1.

Appendix A. Supplementary data

Supplementary material related to this article can be found online at <https://doi.org/10.1016/j.carbon.2025.120117>.

References

- M.H. Müser, Structural lubricity: Role of dimension and symmetry, *Europhys. Lett.* 66 (1) (2004) 97, <http://dx.doi.org/10.1209/epl/i2003-10139-6>.
- S.A. Adelman, J.D. Doll, Generalized langevin equation approach for atom/solid-surface scattering: General formulation for classical scattering off harmonic solids, *J. Chem. Phys.* 64 (6) (1976) 2375–2388, <http://dx.doi.org/10.1063/1.432526>, arXiv:https://pubs.aip.org/aip/jcp/article-pdf/64/6/2375/1890063/2375_1_online.pdf.
- M.H. Müser, L. Wenning, M.O. Robbins, Simple microscopic theory of amontons's laws for static friction, *Phys. Rev. Lett.* 86 (2001) 1295–1298, <http://dx.doi.org/10.1103/PhysRevLett.86.1295>, URL <https://link.aps.org/doi/10.1103/PhysRevLett.86.1295>.
- D. Dietzel, M. Feldmann, U.D. Schwarz, H. Fuchs, A. Schirmeisen, Scaling laws of structural lubricity, *Phys. Rev. Lett.* 111 (2013) 235502, <http://dx.doi.org/10.1103/PhysRevLett.111.235502>, URL <https://link.aps.org/doi/10.1103/PhysRevLett.111.235502>.
- A.S. de Wijn, (In)commensurability, scaling, and multiplicity of friction in nanocrystals and application to gold nanocrystals on graphite, *Phys. Rev. B* 86 (2012) 085429, <http://dx.doi.org/10.1103/PhysRevB.86.085429>, URL <https://link.aps.org/doi/10.1103/PhysRevB.86.085429>.
- H. Gao, M.H. Müser, Structural lubricity of physisorbed gold clusters on graphite and its breakdown: Role of boundary conditions and contact lines, *Front. Chem.* 10 (2022) <http://dx.doi.org/10.3389/fchem.2022.935008>, URL <https://www.frontiersin.org/articles/10.3389/fchem.2022.935008>.
- T.A. Sharp, L. Pastewka, M.O. Robbins, Elasticity limits structural superlubricity in large contacts, *Phys. Rev. B* 93 (2016) 121402, <http://dx.doi.org/10.1103/PhysRevB.93.121402>, URL <https://link.aps.org/doi/10.1103/PhysRevB.93.121402>.
- J.M. Monti, M.O. Robbins, Sliding friction of amorphous asperities on crystalline substrates: Scaling with contact radius and substrate thickness, *ACS Nano* 14 (12) (2020) 16997–17003, <http://dx.doi.org/10.1021/acsnano.0c06241>, arXiv:<https://doi.org/10.1021/acsnano.0c06241>, PMID: 33226231.
- G. He, M.H. Müser, M.O. Robbins, Adsorbed layers and the origin of static friction, *Sci.* 284 (5420) (1999) 1650–1652, <http://dx.doi.org/10.1126/science.284.5420.1650>, arXiv:<https://www.science.org/doi/pdf/10.1126/science.284.5420.1650>, URL <https://www.science.org/doi/abs/10.1126/science.284.5420.1650>.
- J. Annett, G.L.W. Cross, Self-assembly of graphene ribbons by spontaneous self-tearing and peeling from a substrate, *Nature* 535 (2016) 271–275, <http://dx.doi.org/10.1038/nature18304>.
- H. Gao, M.H. Müser, Why liquids can appear to solidify during squeeze-out – even when they don't, *J. Colloid Interface Sci.* 562 (2020) 273–278, <http://dx.doi.org/10.1016/j.jcis.2019.10.097>, URL <https://www.sciencedirect.com/science/article/pii/S0021979719312846>.
- H. Gao, History-dependent stress relaxation of liquids under high-confinement: A molecular dynamics study, *Lubr.* 10 (2) (2022) <http://dx.doi.org/10.3390/lubricants10020015>, URL <https://www.mdpi.com/2075-4442/10/2/15>.
- X. Huang, T. Li, J. Wang, K. Xia, Z. Tan, D. Peng, X. Xiang, B. Liu, M. Ma, Q. Zheng, Robust microscale structural superlubricity between graphite and nanostructured surface, *Nat. Commun.* 14 (2023) 2931, <http://dx.doi.org/10.1038/s41467-023-38680-6>.
- E. Cihan, S. İpek, E. Durgun, M.Z. Baykara, Structural lubricity under ambient conditions, *Nat. Commun.* 7 (2016) 12055, <http://dx.doi.org/10.1038/ncomms12055>.
- H. Deng, M. Ma, Y. Song, Q. He, Q. Zheng, Structural superlubricity in graphite flakes assembled under ambient conditions, *Nanoscale* 10 (2018) 14314–14320, <http://dx.doi.org/10.1039/C7NR09628C>.
- W.H. Oo, H. Gao, M.H. Müser, M.Z. Baykara, Persistence of structural lubricity on contaminated graphite: Rejuvenation, aging, and friction switches, *Nano Lett.* 24 (39) (2024) 12118–12124, <http://dx.doi.org/10.1021/acs.nanolett.4c02883>, arXiv:<https://doi.org/10.1021/acs.nanolett.4c02883>, PMID: 39311444.
- M.H. Müser, Shear thinning in the Prandtl model and its relation to generalized Newtonian fluids, *Lubr.* 8 (4) (2020) <http://dx.doi.org/10.3390/lubricants8040038>, URL <https://www.mdpi.com/2075-4442/8/4/38>.
- H. Gao, M.H. Müser, On the shear-thinning of alkanes, *Tribol. Lett.* 72 (2) (2024) 16, <http://dx.doi.org/10.1007/s11249-023-01813-5>.
- Z. Li, Y. Wang, A. Kozbial, G. Shenoy, F. Zhou, R. McGinley, P. Ireland, B. Morganstein, A. Kunkel, S.P. Surwade, L. Li, H. Liu, Effect of airborne contaminants on the wettability of supported graphene and graphite, *Nat. Mater.* 12 (2013) 925–931, <http://dx.doi.org/10.1038/nmat3709>.
- A. Pálkás, G. Kálvin, P. Vancsó, K. Kandrai, M. Szendrő, G. Németh, M. Németh, Á. Pekker, J.S. Pap, P. Petrik, K. Kamarás, L. Tapasztó, P. Nemes-Incze, The composition and structure of the ubiquitous hydrocarbon contamination on van der waals materials, *Nat. Commun.* 13 (2022) 6770, <http://dx.doi.org/10.1038/s41467-022-34641-7>.
- R. Bai, N.L. Tolman, Z. Peng, H. Liu, Influence of atmospheric contaminants on the work function of graphite, *Langmuir* 39 (34) (2023) 12159–12165, <http://dx.doi.org/10.1021/acs.langmuir.3c01459>, arXiv:<https://doi.org/10.1021/acs.langmuir.3c01459>, PMID: 37581604.
- X.W. Zhou, R.A. Johnson, H.N.G. Wadley, Misfit-energy-increasing dislocations in vapor-deposited CoFe/NiFe multilayers, *Phys. Rev. B* 69 (2004) 144113, <http://dx.doi.org/10.1103/PhysRevB.69.144113>.
- S.J. Stuart, A.B. Tutein, J.A. Harrison, A reactive potential for hydrocarbons with intermolecular interactions, *J. Chem. Phys.* 112 (14) (2000) 6472–6486, <http://dx.doi.org/10.1063/1.481208>, arXiv:https://pubs.aip.org/aip/jcp/article-pdf/112/14/6472/19138014/6472_1_online.pdf.
- M.L.P. Price, D. Ostrovsky, W.L. Jorgensen, Gas-phase and liquid-state properties of esters, nitriles, and nitro compounds with the OPLS-AA force field, *J. Comput. Chem.* 22 (13) (2001) 1340–1352, <http://dx.doi.org/10.1002/jcc.1092>, arXiv:<https://onlinelibrary.wiley.com/doi/pdf/10.1002/jcc.1092>, URL <https://onlinelibrary.wiley.com/doi/abs/10.1002/jcc.1092>.
- S.W.I. Situ, K. Pluhackova, R.A. Böckmann, Optimization of the OPLS-AA force field for long hydrocarbons, *J. Chem. Theory Comput.* 8 (4) (2012) 1459–1470, <http://dx.doi.org/10.1021/ct200908r>, arXiv:<https://doi.org/10.1021/ct200908r>, PMID: 26596756.

- [26] J.A. de la Rosa-Abad, G.J. Soldano, S.J. Mejía-Rosales, M.M. Mariscal, Immobilization of Au nanoparticles on graphite tunnels through nanocapillarity, *RSC Adv.* 6 (2016) 77195–77200, <http://dx.doi.org/10.1039/C6RA16231B>.
- [27] Q. Pu, Y. Leng, X. Zhao, P.T. Cummings, Molecular simulations of stretching gold nanowires in solvents, *Nanotechnol.* 18 (42) (2007) 424007, <http://dx.doi.org/10.1088/0957-4484/18/42/424007>.
- [28] A.P. Thompson, H.M. Aktulga, R. Berger, D.S. Bolintineanu, W.M. Brown, P.S. Crozier, P.J. in 't Veld, A. Kohlmeyer, S.G. Moore, T.D. Nguyen, R. Shan, M.J. Stevens, J. Tranchida, C. Trott, S.J. Plimpton, LAMMPS - a flexible simulation tool for particle-based materials modeling at the atomic, meso, and continuum scales, *Comput. Phys. Comm.* 271 (2022) 108171, <http://dx.doi.org/10.1016/j.cpc.2021.108171>, URL <https://www.sciencedirect.com/science/article/pii/S0010465521002836>.
- [29] R.A. Buckingham, J.E. Lennard-Jones, The classical equation of state of gaseous helium, neon and argon, *Proc. R. Soc. Lond. Ser. A. Math. Phys. Sci.* 168 (933) (1938) 264–283, <http://dx.doi.org/10.1098/rspa.1938.0173>, arXiv: <https://royalsocietypublishing.org/doi/pdf/10.1098/rspa.1938.0173>, URL <https://royalsocietypublishing.org/doi/abs/10.1098/rspa.1938.0173>.
- [30] L.-T. Kong, C. Denniston, M.H. Müser, Y. Qi, Non-bonded force field for the interaction between metals and organic molecules: a case study of olefins on aluminum, *Phys. Chem. Chem. Phys.* 11 (2009) 10195–10203, <http://dx.doi.org/10.1039/B906874K>.
- [31] M.H. Müser, Improved cutoff functions for short-range potentials and the wolf summation, *Mol. Simul.* 48 (15) (2022) 1393–1401, <http://dx.doi.org/10.1080/08927022.2022.2094430>, arXiv: <https://doi.org/10.1080/08927022.2022.2094430>.
- [32] H.A. Lorentz, Ueber die anwendung des satzes vom virial in der kinetischen theorie der gase, *Ann. Phys., Lpz.* 248 (1) (1881) 127–136, <http://dx.doi.org/10.1002/andp.18812480110>, arXiv: <https://onlinelibrary.wiley.com/doi/pdf/10.1002/andp.18812480110>, URL <https://onlinelibrary.wiley.com/doi/abs/10.1002/andp.18812480110>.
- [33] D. Berthelot, Sur le mélange des gaz, *C. R.* 126 (3) (1898) 15.
- [34] J. VandeVondele, M. Krack, F. Mohamed, M. Parrinello, T. Chassaing, J. Hutter, Quickstep: Fast and accurate density functional calculations using a mixed Gaussian and plane waves approach, *Comput. Phys. Comm.* 167 (2) (2005) 103–128, <http://dx.doi.org/10.1016/j.cpc.2004.12.014>, URL <https://www.sciencedirect.com/science/article/pii/S0010465500060615>.
- [35] G. Lippert, J. Hutter, M. Parrinello, A hybrid Gaussian and plane wave density functional scheme, *Mol. Phys.* 92 (3) (1997) 477–488, <http://dx.doi.org/10.1080/002689797170220>.
- [36] J. Hutter, M. Iannuzzi, F. Schiffmann, J. VandeVondele, Cp2k: atomistic simulations of condensed matter systems, *WIREs Comput. Mol. Sci.* 4 (1) (2014) 15–25, <http://dx.doi.org/10.1002/wcms.1159>, URL <https://wires.onlinelibrary.wiley.com/doi/abs/10.1002/wcms.1159>.
- [37] T.D. Kühne, M. Iannuzzi, M. Del Ben, V.V. Rybkin, P. Seewald, F. Stein, T. Laino, R.Z. Khaliullin, O. Schütt, F. Schiffmann, D. Golze, J. Wilhelm, S. Chulkov, M.H. Bani-Hashemian, V. Weber, U. Borštnik, M. Taillefumier, A.S. Jakobovits, A. Lazzaro, H. Pabst, T. Müller, R. Schade, M. Guidon, S. Andermat, N. Holmberg, G.K. Schenter, A. Hehn, A. Bussy, F. Belleflamme, G. Tabacchi, A. Glöß, M. Lass, I. Bethune, C.J. Mundy, C. Plessl, M. Watkins, J. VandeVondele, M. Krack, J. Hutter, CP2k: An electronic structure and molecular dynamics software package - quickstep: Efficient and accurate electronic structure calculations, *J. Chem. Phys.* 152 (19) (2020) 194103, <http://dx.doi.org/10.1063/5.0007045>, arXiv: https://pubs.aip.org/aip/jcp/article-pdf/doi/10.1063/5.0007045/16718133/194103_1_online.pdf.
- [38] M. Dion, H. Rydberg, E. Schröder, D.C. Langreth, B.I. Lundqvist, Van der waals density functional for general geometries, *Phys. Rev. Lett.* 92 (2004) 246401, <http://dx.doi.org/10.1103/PhysRevLett.92.246401>, URL <https://link.aps.org/doi/10.1103/PhysRevLett.92.246401>.
- [39] J. VandeVondele, J. Hutter, Gaussian basis sets for accurate calculations on molecular systems in gas and condensed phases, *J. Chem. Phys.* 127 (11) (2007) 114105, <http://dx.doi.org/10.1063/1.2770708>, arXiv: https://pubs.aip.org/aip/jcp/article-pdf/doi/10.1063/1.2770708/14787836/114105_1_online.pdf.
- [40] S. Goedecker, M. Teter, J. Hutter, Separable dual-space Gaussian pseudopotentials, *Phys. Rev. B* 54 (1996) 1703–1710, <http://dx.doi.org/10.1103/PhysRevB.54.1703>, URL <https://link.aps.org/doi/10.1103/PhysRevB.54.1703>.
- [41] C. Hartwigsen, S. Goedecker, J. Hutter, Relativistic separable dual-space Gaussian pseudopotentials from h to rn, *Phys. Rev. B* 58 (1998) 3641–3662, <http://dx.doi.org/10.1103/PhysRevB.58.3641>, URL <https://link.aps.org/doi/10.1103/PhysRevB.58.3641>.
- [42] J.P. Perdew, K. Burke, M. Ernzerhof, Generalized gradient approximation made simple, *Phys. Rev. Lett.* 77 (1996) 3865–3868, <http://dx.doi.org/10.1103/PhysRevLett.77.3865>, URL <https://link.aps.org/doi/10.1103/PhysRevLett.77.3865>.
- [43] S. Grimme, J. Antony, S. Ehrlich, H. Krieg, A consistent and accurate ab initio parametrization of density functional dispersion correction (DFT-d) for the 94 elements H-pu, *J. Chem. Phys.* 132 (15) (2010) 154104, <http://dx.doi.org/10.1063/1.3382344>, arXiv: https://pubs.aip.org/aip/jcp/article-pdf/doi/10.1063/1.3382344/15684000/154104_1_online.pdf.
- [44] S. Kirkpatrick, C.D. Gelatt, M.P. Vecchi, Optimization by simulated annealing, *Sci.* 220 (4598) (1983) 671–680, <http://dx.doi.org/10.1126/science.220.4598.671>, arXiv: <https://www.science.org/doi/pdf/10.1126/science.220.4598.671>, URL <https://www.science.org/doi/abs/10.1126/science.220.4598.671>.
- [45] W. Oo, M. Baykara, H. Gao, A computational study of cluster dynamics in structural lubricity: Role of cluster rotation, *Tribol. Lett.* 71 (2023) 115, <http://dx.doi.org/10.1007/s11249-023-01785-6>.
- [46] M.S. Daw, M.I. Baskes, Embedded-atom method: Derivation and application to impurities, surfaces, and other defects in metals, *Phys. Rev. B* 29 (1984) 6443–6453, <http://dx.doi.org/10.1103/PhysRevB.29.6443>, URL <https://link.aps.org/doi/10.1103/PhysRevB.29.6443>.
- [47] W.A. Steele, The physical interaction of gases with crystalline solids: I. Gas-solid energies and properties of isolated adsorbed atoms, *Surf. Sci.* 36 (1) (1973) 317–352, [http://dx.doi.org/10.1016/0039-6028\(73\)90264-1](http://dx.doi.org/10.1016/0039-6028(73)90264-1), URL <https://www.sciencedirect.com/science/article/pii/0039602873902641>.
- [48] S. Tsuzuki, A. Fujii, Nature and physical origin of CH/ π interaction: significant difference from conventional hydrogen bonds, *Phys. Chem. Chem. Phys.* 10 (2008) 2584–2594, <http://dx.doi.org/10.1039/B718656H>.
- [49] K.R. Paserba, A.J. Gellman, Kinetics and energetics of oligomer desorption from surfaces, *Phys. Rev. Lett.* 86 (2001) 4338–4341, <http://dx.doi.org/10.1103/PhysRevLett.86.4338>, URL <https://link.aps.org/doi/10.1103/PhysRevLett.86.4338>.
- [50] A.J. Gellman, K.R. Paserba, Kinetics and mechanism of oligomer desorption from surfaces: n-alkanes on graphite, *J. Phys. Chem. B* 106 (51) (2002) 13231–13241, <http://dx.doi.org/10.1021/jp021135p>, arXiv: <https://doi.org/10.1021/jp021135p>.
- [51] E. Londero, E.K. Karlson, M. Landahl, D. Ostrovskii, J.D. Rydberg, E. Schröder, Desorption of n-alkanes from graphene: a van der waals density functional study, *J. Phys.: Condens. Matter.* 24 (42) (2012) 424212, <http://dx.doi.org/10.1088/0953-8984/24/42/424212>.
- [52] K. Kamiya, S. Okada, Energetics and electronic structures of alkanes and polyethylene adsorbed on graphene, *Japan. J. Appl. Phys.* 52 (6S) (2013) 06GD10, <http://dx.doi.org/10.7567/JJAP.52.06GD10>.
- [53] G.C. McGonigal, R.H. Bernhardt, D.J. Thomson, Imaging alkane layers at the liquid/graphite interface with the scanning tunneling microscope, *Appl. Phys. Lett.* 57 (1) (1990) 28–30, <http://dx.doi.org/10.1063/1.104234>, arXiv: https://pubs.aip.org/aip/apl/article-pdf/57/1/28/18477366/28_1_online.pdf.
- [54] R.G. Horn, J.N. Israelachvili, Direct measurement of structural forces between two surfaces in a nonpolar liquid, *J. Chem. Phys.* 75 (3) (1981) 1400–1411, <http://dx.doi.org/10.1063/1.442146>, arXiv: https://pubs.aip.org/aip/jcp/article-pdf/75/3/1400/18929833/1400_1_online.pdf.
- [55] M.-D. Krass, N.N. Gosvami, R.W. Carpick, M.H. Müser, R. Bennewitz, Dynamic shear force microscopy of viscosity in nanometer-confined hexadecane layers, *J. Phys.: Condens. Matter.* 28 (13) (2016) 134004, <http://dx.doi.org/10.1088/0953-8984/28/13/134004>.
- [56] M.E. Fisher, B. Wiodm, Decay of correlations in linear systems, *J. Chem. Phys.* 50 (9) (1969) 3756–3772, <http://dx.doi.org/10.1063/1.1671624>, arXiv: https://pubs.aip.org/aip/jcp/article-pdf/50/9/3756/18862410/3756_1_online.pdf.
- [57] K. Nygård, S. Sarman, K. Hyltegren, S. Chodankar, E. Perret, J. Buitenhuis, J.F. van der Veen, R. Kjellander, Density fluctuations of hard-sphere fluids in narrow confinement, *Phys. Rev. X* 6 (2016) 011014, <http://dx.doi.org/10.1103/PhysRevX.6.011014>, URL <https://link.aps.org/doi/10.1103/PhysRevX.6.011014>.
- [58] E.E. Flater, W.R. Ashurst, R.W. Carpick, Nanotribology of octadecyltrichlorosilane monolayers and silicon: Self-mated versus unmated interfaces and local packing density effects, *Langmuir* 23 (18) (2007) 9242–9252, <http://dx.doi.org/10.1021/la063644e>, arXiv: <https://doi.org/10.1021/la063644e>.
- [59] S.M. Wetterer, D.J. Lavrich, T. Cummings, S.L. Bernasek, G. Scoles, Energetics and kinetics of the physisorption of hydrocarbons on au(111), *J. Phys. Chem. B* 102 (46) (1998) 9266–9275, <http://dx.doi.org/10.1021/jp982338+>, arXiv: <https://doi.org/10.1021/jp982338+>.
- [60] W.H. Oo, P.D. Ashby, M.Z. Baykara, Structural superlubricity at high sliding speeds under ambient conditions, 2024, arXiv: [2407.06971](https://arxiv.org/abs/2407.06971), URL <https://arxiv.org/abs/2407.06971>.
- [61] D. Dietzel, C. Ritter, T. Mönninghoff, H. Fuchs, A. Schirmeisen, U.D. Schwarz, Frictional duality observed during nanoparticle sliding, *Phys. Rev. Lett.* 101 (2008) 125505, <http://dx.doi.org/10.1103/PhysRevLett.101.125505>, URL <https://link.aps.org/doi/10.1103/PhysRevLett.101.125505>.